materials

MDPI

Article

Reasonable Design of MXene-Supported Dual-Atom Catalysts with High Catalytic Activity for Hydrogen Evolution and Oxygen Evolution Reaction: A First-Principles Investigation

Erpeng Wang, Miaoqi Guo, Jian Zhou * and Zhimei Sun *

School of Materials Science and Engineering, Beihang University, Beijing 100191, China
* Correspondence: jzhou@buaa.edu.cn (J.Z.); zmsun@buaa.edu.cn (Z.S.)

Abstract: MXene-supported single-atom catalysts (SACs) for water splitting has attracted extensive attention. However, the easy aggregation of individual metal atoms used as catalytic active centers usually leads to the relatively low loading of synthetic SACs, which limits the development and application of SACs. Herein, by performing first-principles calculations for Pt and 3d transition metal single atoms immobilized on a two-dimensional (2D) $Mo_2TiC_2O_2$ MXene surface, we systematically studied the performance of heterogeneous dual-atom catalysts (h-DACs) in hydrogen evolution reaction (HER) and oxygen evolution reaction (OER). Significantly, h-DACs exhibit higher metal atom loading and more flexible active sites compared to SACs. Benefiting from these features, we found that $Pt/Cu@Mo_2TiC_2O_2$ heterogeneous DACs exhibits excellent HER activity with ultra-low overpotential $|\Delta G_H{}^*|$ (0.04 eV), lower than the corresponding $Pt@Mo_2TiC_2O_2$ (0.14 eV) and $Cu@Mo_2TiC_2O_2$ (0.33 eV) SACs, and even lower than that of Pt (0.09 eV). Meanwhile, $Pt/Ni@Mo_2TiC_2O_2$ exhibits superior OER activity with ultra-low overpotential η^{OER} (0.38 V), lower than that of $Pt@Mo_2TiC_2O_2$ (1.11 V) and $Ni@Mo_2TiC_2O_2$ (0.57 V) SACs, and even lower than that of RuO_2 (0.42 V) and IrO_2 (0.56 V). Our finding paves the way for the rational design of h-DACs for HER and OER with excellent activity, which provides guidance for other catalytic reactions.

Keywords: first-principles calculation; dual-atom catalysts (DACs); hydrogen evolution reaction; oxygen evolution reaction; electrocatalyist

Citation: Wang, E.; Guo, M.; Zhou, J.; Sun, Z. Reasonable Design of MXene-Supported Dual-Atom Catalysts with High Catalytic Activity for Hydrogen Evolution and Oxygen Evolution Reaction: A First-Principles Investigation. *Materials* **2023**, *16*, 1457. https://doi.org/10.3390/ma16041457

Academic Editors: Jiayuan Yu and Junfeng Chen

Received: 30 December 2022
Revised: 5 February 2023
Accepted: 7 February 2023
Published: 9 February 2023

1. Introduction

Water splitting technology is debated as the most prospective and sustainable way to produce hydrogen and oxygen, which involves hydrogen evolution reaction (HER) and oxygen evolution reaction (OER) [1–8]. Up to now, the expensive noble metals or their oxides are still deemed as the best choice to propel these reactions, where Pt is used for HER and RuO_2/IrO_2 is used for OER [9–11]. However, the expensiveness and poor durability restrict their development and commercial applications. Hence, it is of great importance and imminent to explore non-noble metal catalysts with high activity and stability to make the water splitting reaction economical and energy-saving.

Since MXenes was discovered in 2011 [12], a new family of two-dimensional (2D) material rich in early-transition metal carbides, nitrides, or carbonitrides, it has attracted enormous interest in the field of electrocatalysis due to its large specific surface area, high stability, and excellent electronic and thermal conductivity [13–21]. MXenes can generally be synthesized by selective removal of the layer of A elements from its parent phase MAX using various methods. Its general chemical formula can be written as $M_{n+1}AX_n$, where M represents the early transition metals, A is the elements of the group IIIA or IVA, and X is the carbon and/or nitrogen atoms. Numerous experiments and theoretical calculations have confirmed that the outer layers of the nanosheet MXenes are usually terminated by several kinds of functional groups, such as OH, O, or F [22–26]. Surface functional groups can improve the stability of the MXenes substrate, effectively prevent the inner metal layers

from being oxidized, and even ameliorate the interaction strength between the MXenes substrate and hydrogen, thus increasing HER activity. However, the functional groups greatly weaken the adsorption strength with OER intermediates (OH^*, O^*, and OOH^*), which is unfavorable for OER [27,28].

Single-atom catalysts (SACs) have received extensive attention in electrocatalysis in the past few years, owing to their fully exposed active sites, maximum atom utilization, extraordinary reaction selectivity, and adjustable surface electronic structure [29–34]. Particularly, it has been well confirmed that the SACs composed of a single metal atom anchored on MXenes substrate have shown great application potential in both HER and OER [2,28,35]. In these electrochemical reactions, the single metal atom mainly plays two roles, acting as the active center and acting as a cocatalyst to regulate the local surface electronic structures. However, due to the significantly increased surface free energy of SACs, the single atom embedded on the substrates would spontaneously aggregate to form nanoclusters in the preparation and catalytic process, which greatly reduces catalytic active sites. This shortcoming results in relatively low-density single-atom loading in the currently reported synthesized SACs, generally lower than 1.5 wt% [36–40]. Therefore, it is of great significance to increase the loading capacity of single atoms while maintaining the unique properties of SACs.

Heterogeneous double-atom catalysis (h-DACs) containing two different metal atoms overcomes the drawback of low SACs loading. Moreover, owing to the synergistic effect of two metal atoms, a large amount of unsaturated coordination, and more flexible active sites, h-DACs have shown great application prospects in various catalytic reactions, such as the hydrogen evolution reaction, oxygen reduction reaction, and nitrogen reduction reaction [41–45]. However, the underlying mechanism for the synergistic effect between diatoms on h-DACs to enhance the performance of HER and OER is not very clear, which is still an urgent issue to be addressed at present.

Herein, by means of first-principles calculations, we systematically investigated the HER and OER catalytic activities of the h-DACs composed of a noble metal Pt atom and a non-noble transition metal atom (e.g., 3d: Ti, V, Cr, Fe, Co, Ni, Cu, and Zn) supported on the ordered double transition metal MXene ($Mo_2TiC_2O_2$) substrate, which has been successfully prepared experimentally [46]. We confirmed that the synergistic effect of h-DACs effectively improves the catalytic activity for HER and OER, and gained a deeper understanding of the reaction mechanism. The result showed that Pt/Cu@$Mo_2TiC_2O_2$ h-DACs exhibits higher catalytic activity than that of the corresponding Pt@$Mo_2TiC_2O_2$ SACs and Cu@$Mo_2TiC_2O_2$ SACs. Pt/Ni@$Mo_2TiC_2O_2$ h-DACs has great potential in OER, and its OER performance was superior to that of Pt@$Mo_2TiC_2O_2$ SACs and Ni@$Mo_2TiC_2O_2$ SACs. Our work extends the exploration of SACs to h-DACs and lays a referential foundation for designing excellent OER and HER catalysts.

2. Materials and Methods

Spin-polarized density functional theory (DFT) calculations based on first principles were implemented using the Vienna ab initio simulation package code (VASP) [47]. The Perdew-Burke-Ernzerhof (PBE) functional within the generalized gradient approximation (GGA) was applied to describe the electron exchange-correlation interactions [48,49]. The core-valence interactions were described by the projector-augmented plane-wave (PAW) method and the cutoff energy of plane-wave basis was set to be 500 eV in all the computations. The convergence tolerances for residual force and energy on each atom during the structure relaxation were set to 0.01 eV/Å and 10^{-5} eV, respectively. Monkhorst-Pack k-mesh grid settings of $3 \times 3 \times 1$ and $7 \times 7 \times 1$ were used to sample the 2D Brillouin zone for geometry optimizations and electronic structure calculations, respectively. In all DFT calculations, the vacuum layer thickness in the z-direction was set to 25 Å to avoid interlayer interactions and the van der Waals interaction was considered by using the empirical correction DFT-D3 approach [50]. The VASPKIT code was used to postprocess the data calculated by VASP [51].

The Gibbs free energy change (ΔG) of each elementary reaction step of the HER and OER was calculated adopting the computational hydrogen electrode (CHE) method proposed by Nørskov et al. [52]. According to this method, the ΔG of each elementary reaction step can be expressed as

$$\Delta G = \Delta E + \Delta ZPE - T\Delta S + \Delta G_{pH} + \Delta G_U \quad (1)$$

where ΔE is the total energy change of the reaction obtained from DFT calculations; ΔZPE and TΔS are the zero-point energy change and the entropy change, respectively; and T is temperature and was set to 298.15 K (room temperature) in this work. Moreover, $\Delta G_U = -eU$ and $\Delta G_{pH} = -k_B T \ln[H^+] = pH \times k_B T \ln 10$ represent the influence of electrode potential (U) and pH on the ΔG in the electrochemical elementary step, respectively, where e is the elementary charge and k_B is the Boltzmann constant. In this work, the values of both U and pH were assumed to be zero.

The overall reaction scheme of HER could be described as

$$H^+ (aq) + e^- + * \rightarrow H^* \quad (2)$$

$$H^* \rightarrow 0.5\, H_2 (g) + * \quad (3)$$

including three parts, namely the initial state H^+ (aq) + e^-, the intermediate adsorbed H^*, and the final product of $0.5H_2$ (g). Here, $*$ represents the preferable adsorption site of intermediates on the catalyst surface, and g and aq refer to the gas phase and aqueous solution, respectively. In general, the overpotential is used to evaluate the catalytic activity of the catalyst in the electrocatalysis calculations. As for HER, the Gibbs free energy of hydrogen adsorption ($|\Delta G_{H^*}|$) is usually selected as the overpotential to judge the catalytic activity. In general, the catalysts with $|\Delta G_{H^*}|$ values of less than 0.2 eV are considered to have high HER catalytic activity, and the closer the value of $|\Delta G_{H^*}|$ is to 0, the higher the HER catalytic activity.

In the acidic environment, the overall OER could be expressed in Equation (4), and the elementary reactions are listed in Equation (5) to Equation (8) [53]:

$$H_2O (l) \rightarrow O_2 (g) + 4H^+ + 4e^- \quad (4)$$

$$H_2O (l) + * \rightarrow OH^* + H^+ + e^- \quad (5)$$

$$OH^* \rightarrow O^* + H^+ + e^- \quad (6)$$

$$H_2O (l) + O^* \rightarrow OOH^* + H^+ + e^- \quad (7)$$

$$OOH^* \rightarrow O_2 (g) + H^+ + e^- \quad (8)$$

Here, $*$ represents the active site on the catalyst surface, and g and l refer to the gas phase and the liquid phase, respectively.

The free energy changes for the four elementary OER could be expressed as $\Delta G_1 = \Delta G_{OH^*}$, $\Delta G_2 = \Delta G_{O^*} - \Delta G_{OH^*}$, $\Delta G_3 = \Delta G_{OOH^*} - \Delta G_{O^*}$, and $\Delta G_4 = 4.92 - \Delta G_{OOH^*}$.

For the OER, the overpotential can be obtained from the following equation:

$$\eta^{OER} = \max\{\Delta G_1, \Delta G_2, \Delta G_3, \Delta G_4\}/e - 1.23 \quad (9)$$

3. Results and Discussion

3.1. Stability of MXene-Supported Catalysts

First, the adsorption behavior of the single metal Pt embedded on a $Mo_2TiC_2O_2$ substrate was investigated. As far as we know, the O-terminated Mo_2TiC_2 system (denoted as $Mo_2TiC_2O_2$) has been successfully prepared experimentally [46]. Given the weak interaction between the O-terminal functional groups and the OER reactive intermediates (OH^*, O^*, and OOH^*), it is crucial to embed metal atom active sites on the surface of $Mo_2TiC_2O_2$ to enhance the ability to activate the reactive intermediates. Based on previous

studies, MXene-supported mono-metal Pt catalysts generally exhibit superior HER and OER catalytic activity [53–55]. Here, the Pt@$Mo_2TiC_2O_2$ structure was first constructed by considering three possible Pt atom anchoring sites: fcc (F), top (T), and hcp (H) (as shown in Figure 1). Through DFT calculations, we found that for the three constructed Pt@$Mo_2TiC_2O_2$ SACs, the top site structure was the most stable, indicating that adsorption is more likely to occur at this site. To evaluate the catalytic activity of Pt@$Mo_2TiC_2O_2$ SACs for the HER and OER, the Gibbs free energy difference of elementary reaction steps for HER (ΔG_{H^*}) and OER (ΔG_{OH^*}, ΔG_{O^*}, ΔG_{OOH^*}) processes were calculated separately, as shown in Figure 1b,c. It is not difficult to see that Pt@$Mo_2TiC_2O_2$ SACs has superior HER catalytic performance with a low $|\Delta G_{H^*}|$ value of 0.14 eV, close to that of Pt (0.09 eV) [11]. However, the catalytic performance of the OER is not as good as expected, showing a larger overpotential barrier of 1.11 V. Then, by simultaneously loading a 3d transition metal atom (TM = Ti, V, Cr, Fe, Co, Ni, Cu, and Zn) on the surface of Pt@$Mo_2TiC_2O_2$ to adjust the electronic structure, it is expected to effectively improve the catalytic activity of Pt@$Mo_2TiC_2O_2$ for HER and OER. Here, the constructed structures were called heterogeneous double-atom catalysts (denoted as Pt/TM@$Mo_2TiC_2O_2$ h-DACs).

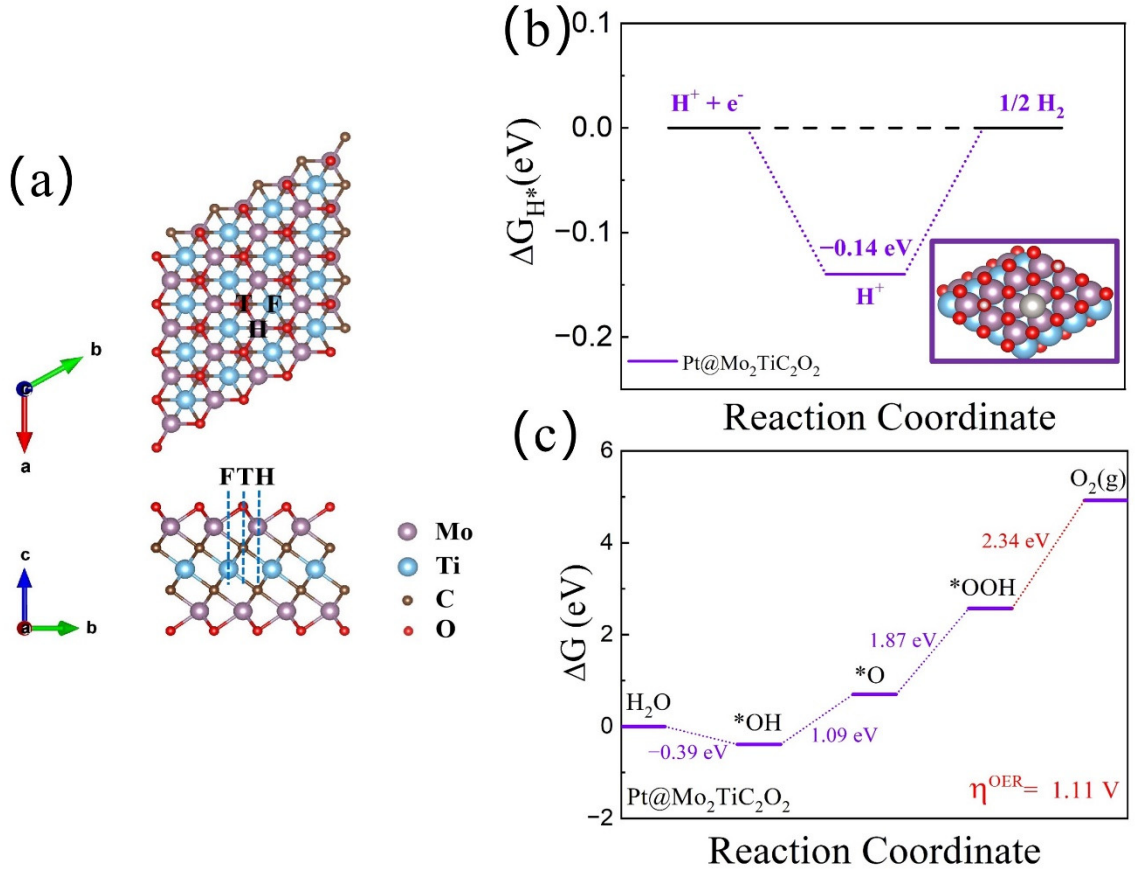

Figure 1. (**a**) Top view and front view of the $Mo_2TiC_2O_2$ and three different single-atom anchoring sites: fcc (F), top (T), and hcp (H). Calculated free energy profile of Pt@$Mo_2TiC_2O_2$ SACs for (**b**) HER and (**c**) OER; the red line represents the energy-consuming step. The "∗" symbol represents the adsorption site. a, b and c are the three directional axes of the cell structure, respectively.

Figure 2 illustrates schematic diagrams of the TM atomic possible adsorption sites on the surface of Pt@$Mo_2TiC_2O_2$, namely Site I, Site II, Site III, Site IV, Site V, and Site VI. The Pt/TM@$Mo_2TiC_2O_2$ h-DAC structures with the lowest surface adsorption energies are depicted in Figure S1. Talking the Pt/Cu@$Mo_2TiC_2O_2$ h-DAC structure as an example, we considered six kinds of possible adsorption sites of the Cu atom, obtained five systems with stable structure after structure optimization, and then selected the configuration with the

lowest total energy for subsequent calculations (see Figure S1). In order to further evaluate the dynamic stability of the above selected systems, ab initio molecular dynamics (AIMD) simulations were implemented at 298 K for 10 ps. For the AIMD simulations, the change in bond length (L) between Cu and Pt atoms and the total energy of h-DACs with time were used to verify the thermal stability (as shown Figure 2b). It can be easily observed that the fluctuation of bond length and total energy was small, indicating that the structure shows high thermodynamic stability.

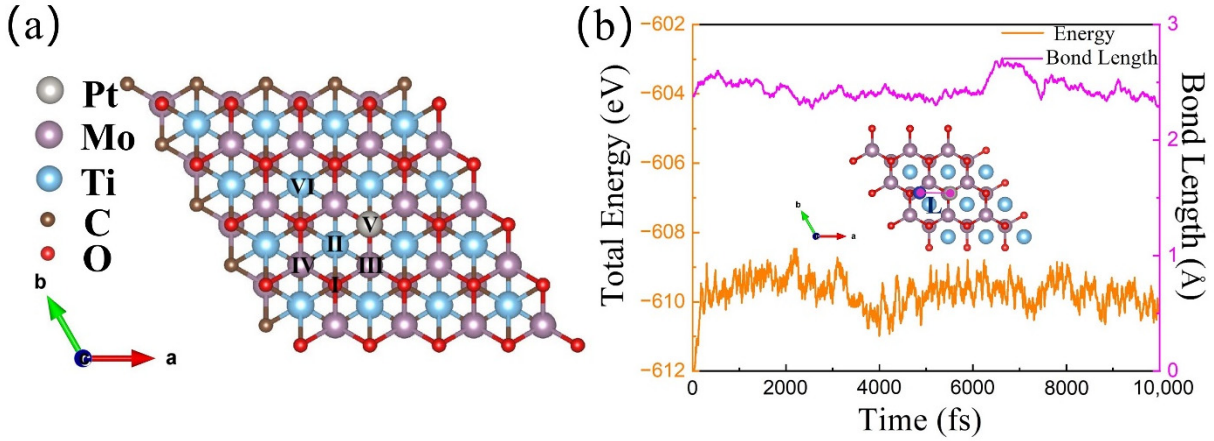

Figure 2. (**a**) The schematic diagrams of the TM atomic possible adsorption sites on the surface of Pt@$Mo_2TiC_2O_2$ (TM = Sc, Ti, V, Cr, Fe, Co, Ni, Cu, and Zn), i.e., Site I, Site II, Site III, Site IV, Site V, and Site VI. (**b**) The evolution of bond length (L) between Cu and Pt atoms and the total energy for Pt/Cu@$Mo_2TiC_2O_2$ h-DACs within 10,000 fs in AIMD simulations performed at 300 K. a, b and c are the three directional axes of the cell structure, respectively.

3.2. HER Catalytic Activity of h-DACs

We first investigated the catalytic activity of Pt/TM@$Mo_2TiC_2O_2$ h-DACs for the HER. Similarly, adequate testing was also required to determine the stable adsorption site of H protons on the h-DACs' surface. For h-DACs, H protons generally tend to be adsorbed on the upper end of O or embedded transition metals, where the embedded transition metal atoms play the role of cocatalyst and catalyst, respectively. Here, Pt/Cu@$Mo_2TiC_2O_2$ h-DACs were also taken as an example to illustrate. As displayed in Figure 3, there are six possible H adsorption sites on the Pt/Cu@$Mo_2TiC_2O_2$ h-DACs' surface, namely Site I, Site II, Site III, Site IV, Site V, and Site VI. The possible adsorption sites of H protons in other studied h-DAC systems are shown in Figure S2. Then, the HER catalytic activity calculations were conducted on these sites. The calculated free energy for H^* adsorption ($\Delta G_H{}^*$) of all the studied h-DACs at different active sites are presented in Table S1 and Figure 3b. It can be seen from Figure 3b that the $|\Delta G_H{}^*|$ values of Pt/Cu@$Mo_2TiC_2O_2$ h-DACs at Site II, Pt/Co@$Mo_2TiC_2O_2$ h-DACs at Site IV, and Pt/V@$Mo_2TiC_2O_2$ h-DACs at Site I are less than 0.2 eV, manifesting excellent HER catalytic activity. It should be noted that the Pt and Cu atoms on Pt/Cu@$Mo_2TiC_2O_2$ (Site II) and Pt and Co atoms on Pt/Co@$Mo_2TiC_2O_2$ (Site IV) are cocatalysts that act as an electron catalytic promoter, while the V atom on Pt/V@$Mo_2TiC_2O_2$ (Site I) is a catalyst that participates in the catalytic reactions. Particularly, Pt/Cu@$Mo_2TiC_2O_2$ has an ultra-low $|\Delta G_H{}^*|$ value of 0.04 eV, even better than that of benchmark Pt (0.09 eV), which probably serves as a promising HER catalyst. For comparison, the HER catalytic activities of the corresponding Pt@$Mo_2TiC_2O_2$ SACs and Cu@$Mo_2TiC_2O_2$ SACs were also tested. The stable H^* adsorption sites and the corresponding free energy for H^* adsorption ($\Delta G_H{}^*$) were displayed in Figure S3. The lowest $|\Delta G_H{}^*|$ values of all adsorption sites for Pt@$Mo_2TiC_2O_2$ (Site III) and Cu@$Mo_2TiC_2O_2$ (Site IV) are 0.14 eV and 0.33 eV, respectively, significantly higher than 0.04 eV for Pt/Cu@$Mo_2TiC_2O_2$, which further indicates that the introduction of double atoms improves the HER catalytic activity of the corresponding SACs.

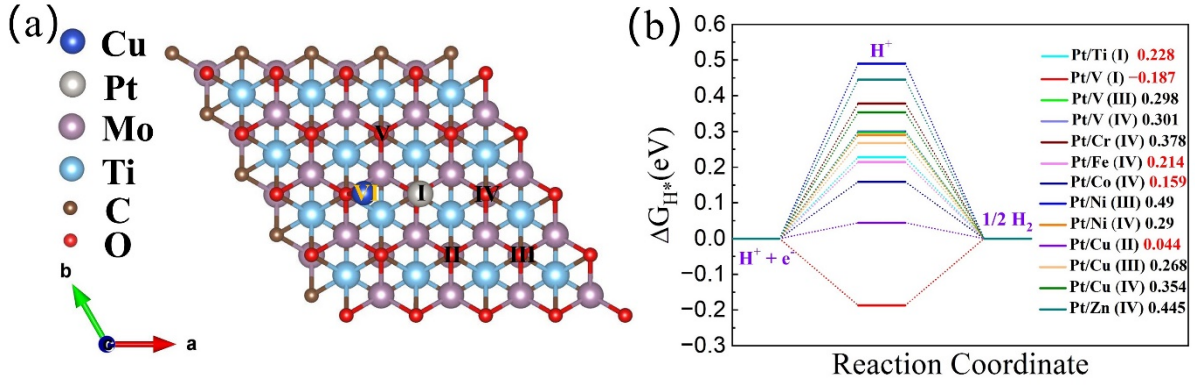

Figure 3. (**a**) Six possible H proton adsorption sites on the Pt/Cu@$Mo_2TiC_2O_2$ h-DACs' surface, i.e., Site I, Site II, Site III, Site IV, Site V, and Site VI. (**b**) Calculated Gibbs free energy profiles of HER at different sites for Pt/TM@$Mo_2TiC_2O_2$ h-DACs (TM = Ti, V, Cr, Fe, Co, Ni, Cu, and Zn). The red numbers represent the catalysts with high HER catalytic activity. a, b and c are the three directional axes of the cell structure, respectively.

3.3. OER Catalytic Activity of h-DACs

We then continued to investigate the OER catalytic activity of these Pt/TM@$Mo_2TiC_2O_2$ h-DACs. The widely accepted entire OER process on SACs can be divided into four stages (see Equations (5)–(8)), which involve three intermediate states (OH*, O*, and OOH*). However, for h-DACs, the OER behavior is more complicated than that of SACs due to the more flexible catalyst active sites. Here, we chose Pt/Ni@$Mo_2TiC_2O_2$ h-DACs as an example to illustrate in detail. All possible reaction paths occurring on Pt/Ni@$Mo_2TiC_2O_2$ h-DACs are displayed in Figure S4, where the energy-favored reaction pathways are marked with red lines. The optimal reaction pathways can be summarized as shown in Figure 4a and described as follows: firstly, the OH* adsorption state was more inclined to spontaneously adsorb to the Pt atom in bare Pt/Ni@$Mo_2TiC_2O_2$ h-DACs accompanied by a −0.62 eV adsorption free energy change. Then, the second OH* was then adsorbed to the Ni atom with the adsorption free energy change of 0.42 eV. Subsequently, the OH* adsorption state on the Ni atom was preferentially transformed into the O* adsorption state, which requires a 1.09 eV reaction energy and releases proton and electron pairs at the same time. Next, it is interesting to note that the subsequent reactions tend to occur only on the Ni single atom to complete the whole four-electron OER reaction process, with the Gibbs free energies of 1.57 eV, 1.61 eV, 1.40 eV, and 0.34 eV required for each elementary reaction separately. In summary, the entire OER on Pt/Ni@$Mo_2TiC_2O_2$ h-DACs can be divided into two stages, namely the $3e^-$ reaction occurring on Ni and Pt atoms (Stage I) and the cyclic OER along the $4e^-$ reaction pathways involving only an Ni atom (Stage II). The OER reaction pathways of other studied Pt/TM@$Mo_2TiC_2O_2$ h-DAC systems are displayed in Figures S5–S11, respectively. From Figure 4b,c, for Pt/Ni@$Mo_2TiC_2O_2$ h-DACs, the formation of OOH* on the Ni atom is the most energy-consuming step, showing the maximum step distance. Furthermore, we found that Pt/Cr@$Mo_2TiC_2O_2$ h-DACs and Pt/Ni@$Mo_2TiC_2O_2$ h-DACs exhibited excellent OER catalytic activity (see Figure 4c and Figure S12), with low overpotentials of 0.49 eV and 0.38 eV, respectively. Especially for Pt/Ni@$Mo_2TiC_2O_2$ h-DACs, the ultra-low overpotential of 0.38 V was obviously lower than the corresponding data for Pt@$Mo_2TiC_2O_2$ SACs (1.11 V) and Ni@$Mo_2TiC_2O_2$ SACs (0.57 V), and even lower than that of RuO_2 (0.42 V) and IrO_2 (0.56 V) [10]. Therefore, Pt/Ni@$Mo_2TiC_2O_2$ h-DACs is promising excellent OER catalysts. Our findings show that the introduction of double atoms can also ameliorate the OER catalytic activity of the corresponding SACs.

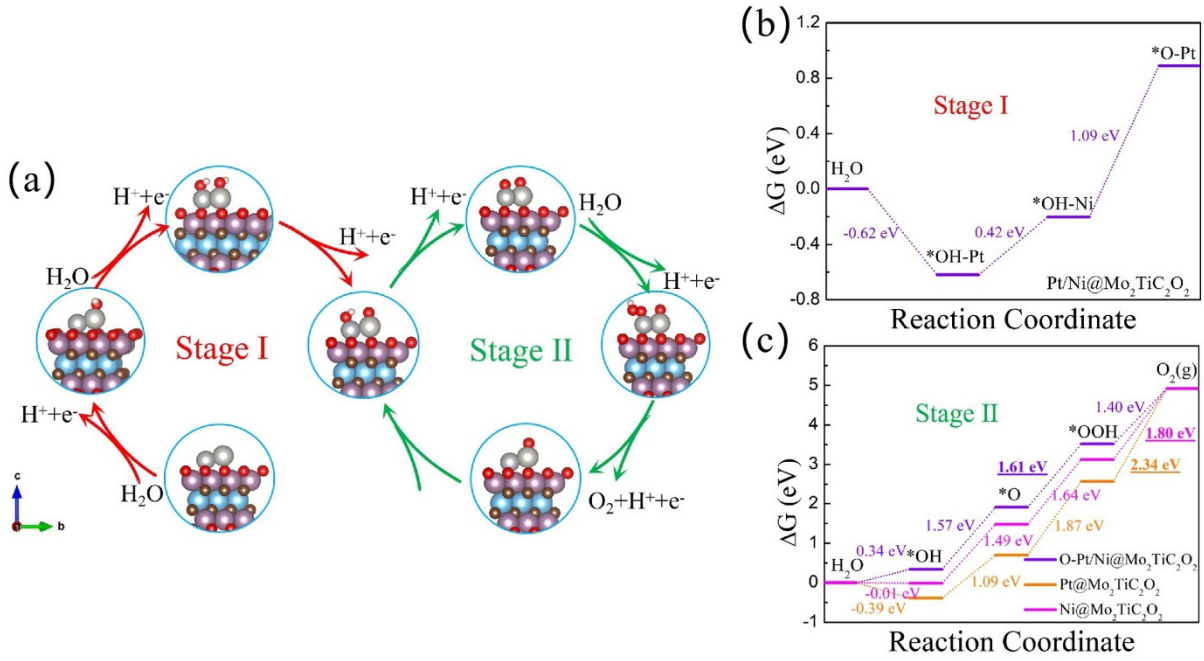

Figure 4. (**a**) The configurations of oxygenated intermediates in energy-favored reaction pathways of OER on Pt/Ni@$Mo_2TiC_2O_2$ h-DACs. The Gibbs free energy diagrams of reaction mechanisms for (**b**) Stage I and (**c**) Stage II and Pt@$Mo_2TiC_2O_2$ SACs and Ni@$Mo_2TiC_2O_2$ SACs. The underlined number represents the most energy-consuming step. The "∗" symbol represents the adsorption site. a, b and c are the three directional axes of the cell structure, respectively.

It is known that good conductivity is the prerequisite for the operation of electrocatalysts, which can be directly observed from its electronic structure. In order to deeply understand the catalytic activity of h-DACs for the OER, we further calculated their electronic density of states (DOS). As shown in Figure S13b, the average DOS per atom states of Pt/Ni@$Mo_2TiC_2O_2$ h-DACs and Pt/Cr@$Mo_2TiC_2O_2$ h-DACs with high OER catalytic activity is continuous at the Fermi level, implying that they are metal-conductive and conducive to electron transport. For the Pt/Ni@$Mo_2TiC_2O_2$ h-DACs, the adsorption of OH^* in the first elementary step and formation of O^* in the second elementary step are the main differences from Ni@$Mo_2TiC_2O_2$ SACs (as shown in Figure 4c). Therefore, we focus on these differences in the subsequent discussion. It is well known that the total Gibbs free energy change for a complete OER progress is 4.92 eV, so the free energy differences for each elementary step of the most ideal OER catalyst should be 1.23 eV. For Ni@$Mo_2TiC_2O_2$ SACs, the sum of the Gibbs free energy change of the first two elementary steps is 1.48 eV, which makes the subsequent two elementary steps need to share the free energy difference of 3.44 eV, resulting in a large overpotential for OER. This situation was well ameliorated on the Pt/Ni@$Mo_2TiC_2O_2$ h-DACs, in which the structure of O-Pt plays an important role. This can be understood from the perspective of d-band center theory. When the adsorbate OH^* binds to the Ni metal atom, the p orbital of the O atom would couple with the d orbital of the Ni atom to form a bonding state and an anti-bonding state (as shown in Figure 5a). The electrons occupying the bonding state make the whole system more stable; on the contrary, the occupation in the anti-bonding state makes the system unstable. The higher (lower) the d-band center of a metal site, the more (less) electrons filled into anti-bonding state, and the stronger (weaker) the affinity with the adsorbate [56]. It can be seen that the synergistic effects of the Pt atom and Ni atom reduce the d-band center of the Ni metal site, especially that the co-adsorbed *O-Pt/Ni@$Mo_2TiC_2O_2$ structure further reduces the position of the d-band center of the Ni metal site (See Figure 5b), which leads to a decrease in the adsorption energy bound to the OH adsorbate. Thus, the free energy change in the first two elementary steps of the OER was effectively improved, thereby reducing

the OER overpotential and remarkably promoting the catalytic activity. Moreover, this result is consistent with that of the Bader charge transfer on the Ni atom, which decreases from −0.89e of Ni@$Mo_2TiC_2O_2$ SACs to −0.79e of Pt/Ni@$Mo_2TiC_2O_2$ h-DACs and further decreases to −0.76e of *O-Pt/Ni@$Mo_2TiC_2O_2$ h-DACs (See Table S2).

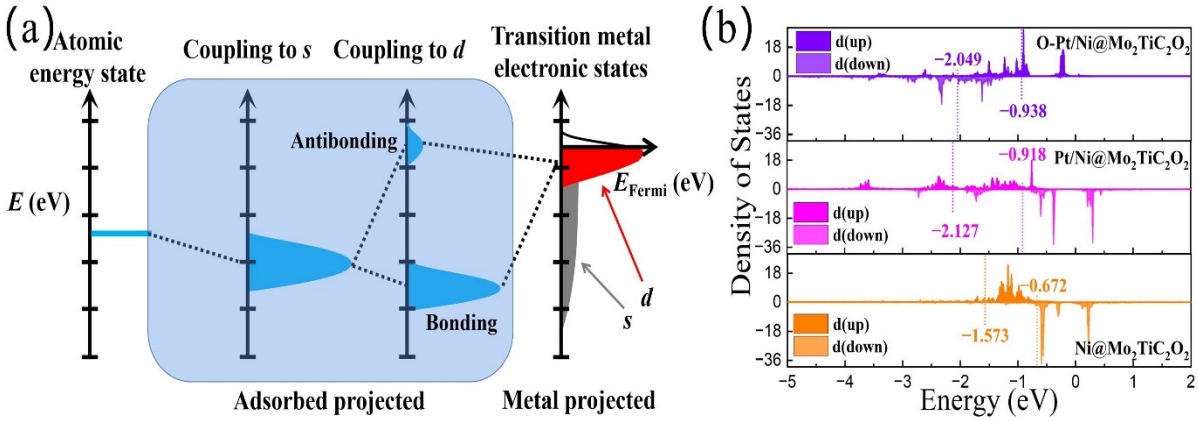

Figure 5. (**a**) The schematic diagram of d-band center theory mechanism. (**b**) The projected DOS and the position of d-band center of Ni atom for Ni@$Mo_2TiC_2O_2$, Pt/Ni@$Mo_2TiC_2O_2$, and O-Pt/Ni@$Mo_2TiC_2O_2$. The position of d-band center of spin-up and spin-down are marked with numbers, respectively.

4. Conclusions

In conclusion, on the basis of the DFT first-principles calculations, we systematically explored the OER and HER catalytic activity of Pt/TM@$Mo_2TiC_2O_2$ heterogeneous double-atom catalysis (TM = Ti, V, Cr, Fe, Co, Ni, Cu, and Zn). Our computations demonstrated that the constructed h-DACs catalysts have more flexible activity centers than the SACs and the h-DACs, which significantly increase the loading of metal atoms. In addition, the synergistic effect of bimetallic atoms of h-DACs enhances the OER and HER catalytic activity of the corresponding SACs. We found that Pt/Cu@$Mo_2TiC_2O_2$, Pt/V@$Mo_2TiC_2O_2$, and Pt/Co@$Mo_2TiC_2O_2$ h-DACs showed great potential in HER catalysis and Pt/Ni@$Mo_2TiC_2O_2$ and Pt/Cr@$Mo_2TiC_2O_2$ h-DACs exhibited superior OER catalytic activity. In particular, two h-DACs, Pt/Cu@$Mo_2TiC_2O_2$ and Pt/Ni@$Mo_2TiC_2O_2$, exhibited ultra-low overpotentials for the HER ($|\Delta G_H{}^*|$ = 0.04 eV) and OER (η^{OER} = 0.38 V), respectively, which are even better than those of the benchmark Pt ($|\Delta G_H{}^*|$ = 0.09 eV) and RuO_2 (η^{OER} = 0.42 V) or IrO_2 (η^{OER} = 0.56 V). Specifically, the formation of the co-adsorbed *O-Pt/Ni@$Mo_2TiC_2O_2$ structure clarifies the origin of the high catalytic activity of Pt/Ni@$Mo_2TiC_2O_2$ h-DACs. Our findings provide a valuable reference for the rational design of catalysts with promising applications for OER and HER.

Supplementary Materials: The following supporting information are available online at https://www.mdpi.com/article/10.3390/ma16041457/s1, Figure S1: The most stable structures diagram for Pt/TM@$Mo_2TiC_2O_2$ h-DACs (TM = Ti, V, Cr, Fe, Co, Ni, Cu and Zn), Figure S2. The possible H proton adsorption sites on the (a) Pt/TM@$Mo_2TiC_2O_2$ h-DACs surface (TM = Ti, V, Cr and Fe); (b) Pt/Co@$Mo_2TiC_2O_2$ h-DACs surface; (c) Pt/Ni@$Mo_2TiC_2O_2$ h-DACs surface; (d) Pt/TM@$Mo_2TiC_2O_2$ h-DACs surface (TM = Cu, Zn), Figure S3. The possible H proton adsorption sites on the (a) Pt@$Mo_2TiC_2O_2$ SACs surface and (b) Cu@$Mo_2TiC_2O_2$ SACs. (c) Calculated Gibbs free energy profiles of HER for Pt@$Mo_2TiC_2O_2$ SACs, Cu@$Mo_2TiC_2O_2$ SACs and Pt/Cu@$Mo_2TiC_2O_2$ h-DACs, Figure S4. The diagram of all possible ORR pathways and corresponding Gibbs free energy on Pt/Ni@$Mo_2TiC_2O_2$ h-DACs, red lines represent the energy-favored reaction pathways, Figure S5. The diagram of all possible ORR pathways and corresponding Gibbs free energy on Pt/Ti@$Mo_2TiC_2O_2$ h-DACs, red lines represent the energy-favored reaction pathways, Figure S6. The diagram of all possible ORR pathways and corresponding Gibbs free energy on Pt/V@$Mo_2TiC_2O_2$ h-DACs, red lines represent the energy-favored reaction pathways, Figure S7. The diagram of all possible ORR pathways and corresponding Gibbs free energy

on Pt/Cr@$Mo_2TiC_2O_2$ h-DACs, red lines represent the energy-favored reaction pathways, Figure S8. The diagram of all possible ORR pathways and corresponding Gibbs free energy on Pt/Fe@$Mo_2TiC_2O_2$ h-DACs, red lines represent the energy-favored reaction pathways, Figure S9. The diagram of all possible ORR pathways and corresponding Gibbs free energy on Pt/Co@$Mo_2TiC_2O_2$ h-DACs, red lines represent the energy-favored reaction pathways, Figure S10. The diagram of all possible ORR pathways and corresponding Gibbs free energy on Pt/Cu@$Mo_2TiC_2O_2$ h-DACs, red lines represent the energy-favored reaction pathways, Figure S11. The diagram of all possible ORR pathways and corresponding Gibbs free energy on Pt/Zn@$Mo_2TiC_2O_2$ h-DACs, red lines represent the energy-favored reaction pathways, Figure S12. The configurations of oxygenated intermediates in energy-favored reactions pathways of OER on Pt/Cr@$Mo_2TiC_2O_2$ h-DACs. The red line represents the most energy-consuming step, Figure S13. (a) The Projected DOS and the location d-band center of Pt atom for Pt@$Mo_2TiC_2O_2$, Pt/Cr@$Mo_2TiC_2O_2$ and Pt-O-Cr@$Mo_2TiC_2O_2$ h-DACs. (b) The electronic DOS (per atom) of Pt/Cr@$Mo_2TiC_2O_2$ h-DACs and Pt/Ni@$Mo_2TiC_2O_2$ h-DACs, Table S1. ΔGH* of different H adsorption sites on the Pt/TM@$Mo_2TiC_2O_2$ DACs surface (TM = Ti, V, Cr, Fe, Co, Ni, Cu and Zn). Wherein, "x" represents structural instability after H proton adsorbed to the site. "-" represents the non-existent sites, Table S2. The number of the charge transfer (Qe, e) from Sigle-atom to substrate.

Author Contributions: Conceptualization, E.W., J.Z. and Z.S.; methodology, E.W., M.G., J.Z. and Z.S.; investigation, E.W. and M.G.; writing—original draft preparation, E.W.; writing—review and editing, E.W., J.Z. and Z.S.; visualization, E.W. and M.G.; funding acquisition, Z.S. All authors have read and agreed to the published version of the manuscript.

Funding: This work was supported by the National Key Research and Development Program of China (2022YFB3807200).

Institutional Review Board Statement: Not applicable.

Informed Consent Statement: Not applicable.

Data Availability Statement: This data presented in this study are available on request from the corresponding authors.

Acknowledgments: We are very grateful for the support of the High-Performance Computing (HPC) resource platform of Beihang University.

Conflicts of Interest: The authors declare no conflict of interest.

References

1. Cheng, Y.; Dai, J.; Song, Y.; Zhang, Y. Nanostructure of Cr_2CO_2 MXene Supported Single Metal Atom as an Efficient Bifunctional Electrocatalyst for Overall Water Splitting. *ACS Appl. Energy Mater.* **2019**, *2*, 6851–6859. [CrossRef]
2. Fu, Z.; Ling, C.; Wang, J. A $Ti_3C_2O_2$ Supported Single Atom, Trifunctional Catalyst for Electrochemical Reactions. *J. Mater. Chem. A* **2020**, *8*, 7801–7807. [CrossRef]
3. Zhang, T.; Zhang, B.; Peng, Q.; Zhou, J.; Sun, Z. Mo_2B_2 MBene-Supported Single-Atom Catalysts as Bifunctional HER/OER and OER/ORR Electrocatalysts. *J. Mater. Chem. A* **2021**, *9*, 433–441. [CrossRef]
4. Ling, C.; Shi, L.; Ouyang, Y.; Zeng, X.C.; Wang, J. Nanosheet Supported Single-Metal Atom Bifunctional Catalyst for Overall Water Splitting. *Nano Lett.* **2017**, *17*, 5133–5139. [CrossRef]
5. Zhang, Y.; Zhu, X.; Zhang, G.; Shi, P.; Wang, A.-L. Rational Catalyst Design for Oxygen Evolution under Acidic Conditions: Strategies toward Enhanced Electrocatalytic Performance. *J. Mater. Chem. A* **2021**, *9*, 5890–5914. [CrossRef]
6. Ahsan, M.A.; He, T.; Eid, K.; Abdullah, A.M.; Curry, M.L.; Du, A.; Santiago, A.R.P.; Echegoyen, L.; Noveron, J.C. Tuning the Intermolecular Electron Transfer of Low-Dimensional and Metal-Free BCN/C_{60} Electrocatalysts via Interfacial Defects for Efficient Hydrogen and Oxygen Electrochemistry. *J. Am. Chem. Soc* **2021**, *143*, 1203–1215. [CrossRef] [PubMed]
7. Lu, Q.; Abdelgawad, A.; Li, J.; Eid, K. Non-Metal-Doped Porous Carbon Nitride Nanostructures for Photocatalytic Green Hydrogen Production. *Int. J. Mol. Sci.* **2022**, *23*, 15129. [CrossRef]
8. Ahsan, M.A.; He, T.; Eid, K.; Abdullah, A.M.; Sanad, M.F.; Aldalbahi, A.; Alvarado-Tenorio, B.; Du, A.; Santiago, A.R.P.; Noveron, J.C. Controlling the Interfacial Charge Polarization of MOF-De-rived 0D−2D vdW Architectures as a Unique Strategy for Bifunctional Oxygen Electrocatalysis. *ACS Appl. Mater. Interfaces* **2022**, *14*, 3919–3929. [CrossRef]
9. Reier, T.; Oezaslan, M.; Strasser, P. Electrocatalytic Oxygen Evolution Reaction (OER) on Ru, Ir, and Pt Catalysts: A Comparative Study of Nanoparticles and Bulk Materials. *ACS Catal.* **2012**, *2*, 1765–1772. [CrossRef]
10. Sanchez Casalongue, H.G.; Ng, M.L.; Kaya, S.; Friebel, D.; Ogasawara, H.; Nilsson, A. In Situ Observation of Surface Species on Iridium Oxide Nanoparticles during the Oxygen Evolution Reaction. *Angew. Chem. Int. Ed.* **2014**, *53*, 7169–7172. [CrossRef]

11. Nørskov, J.K.; Bligaard, T.; Logadottir, A.; Kitchin, J.R.; Chen, J.G.; Pandelov, S.; Stimming, U. Trends in the Exchange Current for Hydrogen Evolution. *J. Electrochem. Soc.* **2005**, *152*, J23–J26. [CrossRef]
12. Naguib, M.; Kurtoglu, M.; Presser, V.; Lu, J.; Niu, J.; Heon, M.; Hultman, L.; Gogotsi, Y.; Barsoum, M.W. Two-Dimensional Nanocrystals Produced by Exfoliation of Ti_3AlC_2. *Adv. Mater.* **2011**, *23*, 4248–4253. [CrossRef] [PubMed]
13. Xiao, Y.; Zhang, W. High Throughput Screening of M_3C_2 MXenes for Efficient CO_2 Reduction Conversion into Hydrocarbon Fuels. *Nanoscale* **2020**, *12*, 7660–7673. [CrossRef]
14. Handoko, A.D.; Chen, H.; Lum, Y.; Zhang, Q.; Anasori, B.; Seh, Z.W. Two-Dimensional Titanium and Molybdenum Carbide MXenes as Electrocatalysts for CO_2 Reduction. *iScience* **2020**, *23*, 101181. [CrossRef]
15. Huang, B.; Li, N.; Ong, W.-J.; Zhou, N. Single Atom-Supported MXene: How Single-Atomic-Site Catalysts Tune the High Activity and Selectivity of Electrochemical Nitrogen Fixation. *J. Mater. Chem. A* **2019**, *7*, 27620–27631. [CrossRef]
16. Gan, J.; Li, F.; Tang, Y.; Tang, Q. Theoretical Study of Transition-Metal-Modified Mo_2CO_2 MXene as a Catalyst for the Hydrogen Evolution Reaction. *ChemSusChem* **2020**, *13*, 6005–6015. [CrossRef] [PubMed]
17. Yu, Y.; Zhou, J.; Sun, Z. Novel 2D Transition-Metal Carbides: Ultrahigh Performance Electrocatalysts for Overall Water Splitting and Oxygen Reduction. *Adv. Funct. Mater.* **2020**, *30*, 2000570. [CrossRef]
18. Zhou, S.; Yang, X.; Pei, W.; Jiang, Z.; Zhao, J. MXene and MBene as Efficient Catalysts for Energy Conversion: Roles of Surface, Edge and Interface. *J. Phys. Energy* **2021**, *3*, 012002. [CrossRef]
19. Eid, K.; Lu, Q.; Abdel-Azeim, S.; Soliman, A.; Abdullah, A.M.; Abdelgwad, A.M.; Forbes, R.P.; Ozoemena, K.I.; Varma, R.S.; Shibl, M.F. Highly exfoliated Ti3C2Tx MXene nanosheets atomically doped with Cu for efficient electrochemical CO_2 reduction: An experimental and theoretical study. *J. Mater. Chem. A* **2022**, *10*, 1965–1975. [CrossRef]
20. Peng, Q.; Rehman, J.; Eid, K.; Alofi, A.S.; Laref, A.; Albaqami, M.D.; Alotabi, R.G.; Shibl, M.F. Vanadium Carbide (V_4C_3) MXene as an Effificient Anode for Li-Ion and Na-Ion Batteries. *Nanomaterials* **2022**, *12*, 2825. [CrossRef]
21. Ibrahim, Y.; Meslam, M.; Eid, K.; Salah, B.; Abdullah, A.M.; Ozoemena, K.I.; Elzatahry, A.; Sharaf, M.; Sillanpää, M. A Review of MXenes as Emergent Materials for Dye Removal from Wastewater. *Sep. Purif. Technol.* **2022**, *282*, 120083. [CrossRef]
22. Luo, Y.; Chen, G.-F.; Ding, L.; Chen, X.; Ding, L.-X.; Wang, H. Efficient Electrocatalytic N_2 Fixation with MXene under Ambient Conditions. *Joule* **2019**, *3*, 279–289. [CrossRef]
23. Lu, C.; Yang, L.; Yan, B.; Sun, L.; Zhang, P.; Zhang, W.; Sun, Z. Nitrogen-Doped Ti_3C_2 MXene: Mechanism Investigation and Electrochemical Analysis. *Adv. Funct. Mater.* **2020**, *30*, 2000852. [CrossRef]
24. Shahzad, F.; Iqbal, A.; Kim, H.; Koo, C.M. 2D Transition Metal Carbides (MXenes): Applications as an Electrically Conducting Material. *Adv. Mater.* **2020**, *32*, 2002159. [CrossRef]
25. Gogotsi, Y.; Anasori, B. The Rise of MXenes. *ACS Nano* **2019**, *13*, 8491–8494. [CrossRef]
26. Anasori, B.; Lukatskaya, M.R.; Gogotsi, Y. 2D Metal Carbides and Nitrides (MXenes) for Energy Storage. *Nat. Rev. Mater.* **2017**, *2*, 16098. [CrossRef]
27. Pang, J.; Mendes, R.G.; Bachmatiuk, A.; Zhao, L.; Ta, H.Q.; Gemming, T.; Liu, H.; Liu, Z.; Rummeli, M.H. Applications of 2D MXenes in Energy Conversion and Storage Systems. *Chem. Soc. Rev.* **2019**, *48*, 72–133. [CrossRef]
28. Kan, D.; Wang, D.; Zhang, X.; Lian, R.; Xu, J.; Chen, G.; Wei, Y. Rational Design of Bifunctional ORR/OER Catalysts Based on Pt/Pd-Doped Nb_2CT_2 MXene by First-Principles Calculations. *J. Mater. Chem. A* **2020**, *8*, 3097–3108. [CrossRef]
29. Zhang, M.; Du, J.; Chen, Y. Single Cu Atom Supported on Modified H-BN Monolayer as n-p Co-doped Catalyst for CO Oxidation: A Computational Study. *Catal. Today* **2021**, *368*, 148–160. [CrossRef]
30. Lei, Y.; Wang, Y.; Liu, Y.; Song, C.; Li, Q.; Wang, D.; Li, Y. Designing Atomic Active Centers for Hydrogen Evolution Electrocatalysts. Angew. *Chem. Int. Ed.* **2020**, *59*, 20794–20812. [CrossRef]
31. Ouyang, Y.; Ling, C.; Chen, Q.; Wang, Z.; Shi, L.; Wang, J. Activating Inert Basal Planes of MoS_2 for Hydrogen Evolution Reaction through the Formation of Different Intrinsic Defects. *Chem. Mater.* **2016**, *28*, 4390–4396. [CrossRef]
32. Jung, E.; Shin, H.; Lee, B.-H.; Efremov, V.; Lee, S.; Lee, H.S.; Kim, J.; Hooch Antink, W.; Park, S.; Lee, K.-S.; et al. Atomic-Level Tuning of Co–N–C Catalyst for High-Performance Electrochemical H_2O_2 Production. *Nat. Mater.* **2020**, *19*, 436–442. [CrossRef] [PubMed]
33. Kour, G.; Mao, X.; Du, A. Single Copper Atoms Supported on ZnS as an Efficient Catalyst for Electrochemical Reduction of CO to CH_3OH. *ChemNanoMat* **2020**, *6*, 1806–1811. [CrossRef]
34. Xu, H.; Wang, D.; Yang, P.; Liu, A.; Li, R.; Li, Y.; Xiao, L.; Ren, X.; Zhang, J.; An, M. Atomically Dispersed M–N–C Catalysts for the Oxygen Reduction Reaction. *J. Mater. Chem. A* **2020**, *8*, 23187–23201. [CrossRef]
35. Chen, Z.; Fan, X.; Shen, Z.; Ruan, X.; Wang, L.; Zeng, H.; Wang, J.; An, Y.; Hu, Y. Cu Anchored Ti_2NO_2 as High Performance Electrocatalyst for Oxygen Evolution Reaction: A Density Functional Theory Study. *ChemCatChem* **2020**, *12*, 4059–4066. [CrossRef]
36. Choi, C.H.; Kim, M.; Kwon, H.C.; Cho, S.J.; Yun, S.; Kim, H.-T.; Mayrhofer, K.J.J.; Kim, H.; Choi, M. Tuning Selectivity of Electrochemical Reactions by Atomically Dispersed Platinum Catalyst. *Nat. Commun.* **2016**, *7*, 10922. [CrossRef]
37. Li, J.; Chen, S.; Yang, N.; Deng, M.; Ibraheem, S.; Deng, J.; Li, J.; Li, L.; Wei, Z. Ultrahigh-Loading Zinc Single-Atom Catalyst for Highly Efficient Oxygen Reduction in Both Acidic and Alkaline Media. *Angew. Chem. Int. Ed.* **2019**, *58*, 7035–7039. [CrossRef]
38. Liu, P.; Zhao, Y.; Qin, R.; Mo, S.; Chen, G.; Gu, L.; Chevrier, D.M.; Zhang, P.; Guo, Q.; Zang, D.; et al. Photochemical Route for Synthesizing Atomically Dispersed Palladium Catalysts. *Science* **2016**, *352*, 797–800. [CrossRef]
39. Song, P.; Luo, M.; Liu, X.; Xing, W.; Xu, W.; Jiang, Z.; Gu, L. Zn Single Atom Catalyst for Highly Efficient Oxygen Reduction Reaction. *Adv. Funct. Mater.* **2017**, *27*, 1700802. [CrossRef]

40. Wu, Z.-Y.; Xu, X.-X.; Hu, B.-C.; Liang, H.-W.; Lin, Y.; Chen, L.-F.; Yu, S.-H. Iron Carbide Nanoparticles Encapsulated in Mesoporous Fe-N-Doped Carbon Nanofibers for Efficient Electrocatalysis. *Angew. Chem. Int. Ed.* **2015**, *54*, 8179–8183. [CrossRef]
41. Bai, L.; Hsu, C.-S.; Alexander, D.T.L.; Chen, H.M.; Hu, X. Double-Atom Catalysts as a Molecular Platform for Heterogeneous Oxygen Evolution Electrocatalysis. *Nat. Energy* **2021**, *6*, 1054–1066. [CrossRef]
42. Kong, F.; Si, R.; Chen, N.; Wang, Q.; Li, J.; Yin, G.; Gu, M.; Wang, J.; Liu, L.-M.; Sun, X. Origin of Hetero-Nuclear Au-Co Dual Atoms for Efficient Acidic Oxygen Reduction. *Appl. Catal. B Environ.* **2022**, *301*, 120782. [CrossRef]
43. Wei, B.; Fu, Z.; Legut, D.; Germann, T.C.; Du, S.; Zhang, H.; Francisco, J.S.; Zhang, R. Rational Design of Highly Stable and Active MXene-Based Bifunctional ORR/OER Double-Atom Catalysts. *Adv. Mater.* **2021**, *33*, 2102595. [CrossRef] [PubMed]
44. Zhang, J.; Huang, Q.; Wang, J.; Wang, J.; Zhang, J.; Zhao, Y. Supported Dual-Atom Catalysts: Preparation, Characterization, and Potential Applications. *Chin. J. Catal.* **2020**, *41*, 783–798. [CrossRef]
45. Zhang, L.; Si, R.; Liu, H.; Chen, N.; Wang, Q.; Adair, K.; Wang, Z.; Chen, J.; Song, Z.; Li, J.; et al. Atomic Layer Deposited Pt-Ru Dual-Metal Dimers and Identifying Their Active Sites for Hydrogen Evolution Reaction. *Nat. Commun.* **2019**, *10*, 4936. [CrossRef] [PubMed]
46. Zhang, J.; Zhao, Y.; Guo, X.; Chen, C.; Dong, C.-L.; Liu, R.-S.; Han, C.-P.; Li, Y.; Gogotsi, Y.; Wang, G. Single Platinum Atoms Immobilized on an MXene as an Efficient Catalyst for the Hydrogen Evolution Reaction. *Nat. Catal.* **2018**, *1*, 985–992. [CrossRef]
47. Kresse, G.; Furthmüller, J. Efficient Iterative Schemes for Ab Initio Total-Energy Calculations Using a Plane-Wave Basis Set. *Phys. Rev. B* **1996**, *54*, 11169–11186. [CrossRef]
48. Perdew, J.P.; Wang, Y. Accurate and Simple Analytic Representation of the Electron-Gas Correlation Energy. *Phys. Rev. B* **1992**, *45*, 13244–13249. [CrossRef]
49. Perdew, J.P.; Burke, K.; Ernzerhof, M. Generalized Gradient Approximation Made Simple. *Phys. Rev. Lett.* **1996**, *77*, 3865–3868. [CrossRef]
50. Moellmann, J.; Grimme, S. DFT-D3 Study of Some Molecular Crystals. *J. Phys. Chem. C* **2014**, *118*, 7615–7621. [CrossRef]
51. Wang, V.; Xu, N.; Liu, J.-C.; Tang, G.; Geng, W.-T. VASPKIT: A User-Friendly Interface Facilitating High-Throughput Computing and Analysis Using VASP Code. *Comput. Phys. Commun.* **2021**, *267*, 108033. [CrossRef]
52. Nørskov, J.K.; Rossmeisl, J.; Logadottir, A.; Lindqvist, L.; Kitchin, J.R.; Bligaard, T.; Jónsson, H. Origin of the Overpotential for Oxygen Reduction at a Fuel-Cell Cathode. *J. Phys. Chem. B* **2004**, *108*, 17886–17892. [CrossRef]
53. Wang, E.; Zhang, B.; Zhou, J.; Sun, Z. High Catalytic Activity of MBenes-Supported Single Atom Catalysts for Oxygen Reduction and Oxygen Evolution Reaction. *Appl. Surf. Sci.* **2022**, *604*, 154522. [CrossRef]
54. Jing, T.; Liang, D.; Hao, J.; Deng, M.; Cai, S. Single Pt Atoms Stabilized on $Mo_2TiC_2O_2$ for Hydrogen Evolution: A First-Principles Investigation. *J. Chem. Phys.* **2019**, *151*, 024702. [CrossRef]
55. Kan, D.; Lian, R.; Wang, D.; Zhang, X.; Xu, J.; Gao, X.; Yu, Y.; Chen, G.; Wei, Y. Screening Effective Single-Atom ORR and OER Electrocatalysts from Pt Decorated MXenes by First-Principles Calculations. *J. Mater. Chem. A* **2020**, *8*, 17065–17077. [CrossRef]
56. Huang, H.; Jia, H.; Liu, Z.; Gao, P.; Zhao, J.; Luo, Z.; Yang, J.; Zeng, J. Understanding of Strain Effects in the Electrochemical Reduction of CO_2: Using Pd Nanostructures as an Ideal Platform. *Angew. Chem. Int. Ed.* **2017**, *56*, 3594–3598. [CrossRef]